PCCP

Accepted Manuscript

ROYAL SOCIETY OF CHEMISTRY

www.rsc.org/pccp

PCCP

ARTICLE

Case Study of the Interplay of Manganese and Nitrate in Hydroxyapatite Nanoparticles: Association of Oppositely Charged Impurities as Revealed by Pulsed EPR and DFT

Received 00th January 20xx,
Accepted 00th January 20xx

DOI: 10.1039/x0xx00000x

www.rsc.org/

Marat Gafurov[a,] †, Timur Biktagirov[a], Georgy Mamin[a], Elena Klimashina[b], Valery Putlayev[b], L. Kuznetsova[c], Sergei Orlinskii[a]

The interplay of oppositely charged substitutions in the structure of hydroxyapatite (HAp) nanopowders is investigated on atomic level by pulsed electron paramagnetic (EPR) technique and *ab initio* density functional theory calculations. Benefits of EPR to determine Mn^{2+} ions in nano-HAp samples are demonstrated. A simple approach based on the measurements of electron spin relaxation times allowed observing the strong influence of fast-relaxing Mn^{2+} ions on the relaxation characteristics of the nitrate ions (NO_3^-/NO_3^{2-}) incorporated in trace amounts. Based on the results of *ab initio* calculations, we show the propensity of Mn^{2+} and NO_3^-/NO_3^{2-} to associate within HAp crystal lattice. This could have a direct impact on the functional properties of the material especially related to the resorption and ion exchange. Furthermore, such an effect can increase a propensity of undesired impurities to incorporate into the doped nanocrystals.

1. Introduction

More than 30 years ago hydroxyapatite ($Ca_{10}(PO_4)_6(OH)_2$; HAp) has been recognized as a promising biomaterial. Now it finds various applications: as a material for bone implant surgery [1-3], as a vehicle for bio-imaging and therapeutic delivery [4, 5], in chemical engineering [6-8], etc. HAp can be quite easily synthesized in the form of nanocrystals doped by various ionic species, thereby obtaining desired functionality and biocompatibility of the material. For this reason, the mechanisms of uptake and release of substitutional ions attract a great interest of the researchers. Among all the possible substitutions divalent cationic additives (transition metals Zn^{2+}, Co^{2+}, Cu^{2+}, Mn^{2+}, alkaline earths and other metals of the II-nd group of the Periodic Table) are of particular importance [9]. These dopants can either alternate physicochemical properties of the material and its surface (solubility, mechanical strength, etc.), or directly induce biological response when released in the host environment via ion exchange pathway.

There are numerous theoretical and experimental studies devoted to the thermodynamics of ion exchange and uptake with the special attention on the functional characteristics of the material [10-12]. However, the existing models usually do not consider a possible influence of the lattice defects (including those that are created by other additives) on the distribution of divalent ions within the crystal, their uptake and release. Since HAp always contains a certain level of intrinsic defects and impurities that appears to be a relevant issue. On the other hand, one can expect that the propensity of defects or undesired impurities (which also can be potentially harmful) to incorporate into the modified HAp might differ from the case of pure HAp material. Therefore, it is quite important to be able to characterize and predict a mutual impact of different ionic substitutions within HAp crystals and to understand the underlying mechanisms.

Only few works providing an atomic-level insight on the problem exist. The recent work by Matsunaga *et al*. contains a detailed discussion of a tendency of substitutional Zn^{2+} ion to associate with charge-neutral Ca^{2+} vacancy defect complex [13]. Another related issue is concerned in [14] in which the propensity of the segregation of Mg^{2+} ions (instead of uniform distribution) within the lattice is proposed. There are several publications describing the effects of HAp co-doping by Mg^{2+} and CO_3^{2-} [15], Zn^{2+} and CO_3^{2-} [16], Sr^{2+} and CO_3^{2-} [17], Mg^{2+}, Sr^{2+} and Mn^{2+} [18] on the functional characteristics of HAp. To our knowledge, the issue is still poorly explored, especially for the case of nanosized material.

The vast majority of the works devoted to the doping of nanostructures are focused on the semiconducting materials [19, 20]. In general, doping of nanocrystals is widely appreciated to be a very challenging problem (for example, due to self-purification mechanisms). In this sense, for effective development and production of functional nanostructured materials understanding the fundamental process of doping is mandatory. This objective is often

[a] Kazan Federal University, Institute of Physics, 420008 Kazan, Russian Federation.
[b] Lomonosov Moscow State University, Faculty of Material Science, 119992 Moscow, Russian Federation.
[c] Kazan State University for Architecture and Civil Engineering, 420043 Kazan, Russian Federation.
† Corresponding author. E-mail: marat.gafurov@kpfu.ru

addressed to and successfully treated by theoretical analysis [19].

On the other hand, theoretical studies and calculations should be supported experimentally. It motivates the search for reliable analytical methods of characterization of the novel nanostructures including HAp-based materials. Electron paramagnetic/spin resonance (EPR/ESR) has been proven as a powerful analytical tool for apatites studies [21-25]. In our recent papers [26-30] we have exploited the capabilities (mainly the increased sensitivity and resolution) of the modern commercial equipment along with the such techniques as pulsed (Fourier transformed, FT) EPR, relaxation measurements and pulsed electron-nuclear double resonance (ENDOR) to extend the boundaries of the EPR methods for characterization of the nano-HAp containing species. We have shown that when supported with an appropriate computational approach, EPR spectroscopy can not only provide unique information about the chemical and electronic structure of a defect or an impurity in crystal lattice but also shed light on physical properties and composition of the crystalline environment.

In this work we show the capabilities of an approach based on the combination of the pulsed EPR methods and first-principles calculations on a specific case of simultaneous incorporation of oppositely charged ions in nanosized HAp. Namely, we study the interplay of substitutional Mn^{2+} ions with nitrate NO_3^- / NO_3^{2-} anionic impurity.

We focus on manganese since it is a one of the proposed additives for HAp to improve its osteoconductivity and to promote bone formation (see [31] for the recent review on this issue). It is also known that for Mn in different types of crystals electron paramagnetic resonance reveals spin interactions that are sensitive to the local environment of the impurity [20]. The radiation-induced paramagnetic defect, NO_3^{2-}, which can be easily formed under X-ray, ultraviolet, γ or some other type of irradiation of the samples grown by the wet precipitation techniques from the nitrate-containing solutions, has well-established spectroscopic parameters [28-30, 32, 33] and its structure is found to be similar to that of B-type carbonate CO_3^{2-} impurity, which is a most abundant substitution in HAp of great biological relevance [29]. This motivates the use of NO_3^- / NO_3^{2-} as a model of anionic substitution introduced in trace amount to probe the expected Thus we examine the impact of paramagnetic Mn^{2+} ions on the spectral and relaxation characteristics of NO_3^{2-} radical and support the experimental results by density functional theory (DFT) calculations. Based on the obtained results, we discuss a possible role of anionic impurities present in HAp in uptake and release of divalent metal ions during mineralization or ion exchange.

2. Materials and Methods

2.1. Experiment

Mn^{2+}-containing HAp samples with the chemical formula $Ca_{10-0.005}Mn_{0.005}(PO_4)_6(OH)$ (Mn-HAp) and the average size of crystallites of about 30(10) nm were synthesized by the wet precipitation technique. Calcium nitrate monohydrate $Ca(NO_3)_2 \bullet H_2O$ (235 g) was dissolved in 420 ml of 20% NH_4OH (Solution A) while $(NH_4)_2HPO_4$ (72.2 g) was dissolved in 380 ml of deionized water (Solution B). After the $(NH_4)_2HPO_4$ was completely dissolved, 30 ml of 20% NH_4OH was added. Mn-containing reagent ($MnSO_4 \bullet H_2O$) was dissolved in 100 ml of deionized water and then added to the A solution. The B solution was then added to the Mn-containing A solution and mixed by a magnetic stirrer for 24 h. After mixing, the precipitate was allowed to age for 48 h. Subsequently, the supernatant was decanted and then washed with 2.5 l of deionized water three times to remove the excess of NH_4OH and NO_3^-. The washing procedure was repeated three times. After washing, the MnHA precipitate was separated from the liquid by filtering through Buhner funnel. A part of the MnHA precipitate was heated at 900°C for 3 h to remove residual NH_4NO_3 and improve sample crystallinity. The powders of nanosized HAp containing only nitrate impurity (hereinafter denoted as “pure HAp” or just HAp) was prepared by the same technique as described in [34].

X-ray diffraction (XRD) analysis (D2 Phaser diffractometer, Bruker) shows that all the samples contain only one phase with the parameters of the unit cell typical for the bulk crystals of the hydroxyapatite. Sizes of crystallites (30 nm) were extracted from X-ray diffraction line profile (002) using Scherrer- and Wilson-formulas from Williamson-Hall-plots according to the procedure of de Keijser, Langford, Mittemeijer *et al* [35].

The micromorphology of the powders was examined by scanning and transmission electron microscopy (JEM-2000FX II, JEOL, operated at 200 kV; and FESEM LEO SUPRA 50VP, Carl Zeiss, 5 kV). It is consistent with the XRD outcomes and with the results of [34]: the nano-particles were grown mainly in the form of needles having an average length of 30(10) nm and cross-sectional size of less than 10 nm. Because the HAp cell volume is about 1 nm^3 [29] it means that one 40 nm $\times$10 nm $\times$ 10 nm cuboid-shaped nano-particle contains about 4000 unit cells that is obviously the upper bound for the studied nanostructures.

The chemical content of the powders was proved by EDS (INCA Energy+, Oxford Instruments, attached to LEO SUPRA 50 VP) and ICP-MS (ELAN - DRC II, Perkin Elmer). The formula $Ca_{10-0.005}Mn_{0.005}(PO_4)_6(OH)$ defines the upper limit of 20 manganese ions per one nano-particle (assuming the uniform distribution among the nano-particles).

As it was shown previously [28-30], the exploited synthesis procedure leads to the incorporation of NO_3^- ion into the HAp lattice (most probably substituting PO_4^{3-} group). The stable NO_3^{2-} paramagnetic center can be produced by X-ray irradiation. In the present work the irradiation of the synthesized nanopowders was performed using URS-55 tube (U = 55kV, I = 16mA, W - anticathode) at room temperature with the estimated dose of 10 kGy. Such high dose allows us to suggest that all possible NO_3^- ions are ionized (cf. with our results in [28-30]).

Pulsed and continuous wave EPR measurements were done using combined X-band (9 GHz) and W-band (94 GHz) Bruker

Elexsys 580/680 spectrometer equipped with the liquid helium temperature controller. Electron spin echo (ESE) EPR spectra were recorded by means of field-swept two-pulse echo sequence π/2 – tau – π with the pulse length of π pulse of 16 (X-band) or 36 ns (W-band), correspondingly, and time delay tau = 240 ns. For the phase-memory time measurements tau was varied from 200 ns up to the desired value with the minimal possible step of 4 ns. The Inversion-Recovery pulse sequence π– T_{delay} – π/2 – tau – π, where π pulse is defined above and T_{delay} was varied, for the spin-lattice relaxation times measurements was used. To separate the contributions from the paramagnetic centers with different electronic spins (S=1/2 and S = 5/2), we have changed the incident microwave power by switching the high power attenuation (HPA) between 7 dB and 16 dB, correspondingly.

2.2. DFT calculations

We employ the plane-wave pseudopotential approach with Perdew-Burke-Ernzerhof version of the generalized gradient approximation of the exchange-correlation functional (GGA-PBE) [36] and Vanderbilt ultrasoft pseudopotentials [37] as implemented in the Quantum ESPRESSO package [38]. The calculations were performed using 88-atom HAp supercell (1×1×1 monoclinic cell; space group $P2_1/b$) with 2×2×1 Monkhorst-Pack k-point mesh [39] and the energy cutoffs of 40 Ry for the smooth part of the electron wave functions and 320 Ry for the augmented electron density. The initial positional parameters for pure HAp were taken from [40]. Before computing the quantities of interest, the structures were allowed to fully relax. The convergence of the supercell size was analyzed by the test calculations using 176-atom HAp configurations (1×2×1 monoclinic cell). Since it is known that GGA-PBE approach has limited accuracy in treatment of strongly localized *d* electrons, we employ DFT+U method which includes additional Coulomb repulsion for Mn^{2+} *3d* shell [41, 42]. The Hubbard-type Coulomb repulsion *U* was set to 3 eV as followed from the linear response analysis [43, 44] performed in this work. Even though we found that use of both U = 0 and U = 3 eV leads to qualitatively similar trends in defect energetic, only the case of U = 3 eV is discussed in the work.

3. Results and Discussion

3.1. ESE EPR of Mn^{2+} in the nanosized powders

Before the X-ray irradiation pure HAp samples are EPR silent. For Mn-HAp samples a broad line at 9 GHz (X-band) is observed (see the next Section 3.2) that is obviously due to the presence of manganese. Indeed, even in the perfect bulk crystals the EPR spectra of Mn^{2+} are very complicated due to the fine structure of the electronic states (electronic spin S = 5/2), strong hyperfine interaction of electron spin with ^{55}Mn nuclear spin I=5/2 and perceptible quadrupole moment of ^{55}Mn nuclei [45-47]. Furthermore, in the nanosized samples the EPR lines broaden causing spectral overlap.

At the same time, the spectrum is well resolved in the ESE W-band experiments (see Fig. 1). The six line pattern with the value of g-factor g = 2.001(1) and hyperfine splitting typical for ions embedded into the crystal structure of powder samples of $A_{hf} \approx 9.1(1)$ mT clearly indicates the presence of manganese in 2+ charge state.

It is worth noting that quantitative determination of manganese in calcified materials including bone and teeth is still a challenge for the analytical tools because of the structural and chemical complexity of the investigated matrix [48]. The benefits of the commercial W-band EPR instrument for the determination and quantification of manganese starting from ppm and sub-ppm levels in the apatite-like minerals was demonstrated in [49]. We show that EPR in the pulsed mode could be used for the non-destructive studies of the manganese containing HAp species. In this sense modern EPR spectroscopy, in our opinion, should be considered as an additional powerful method for the comprehensive analysis of the calcified tissues (materials) [50].

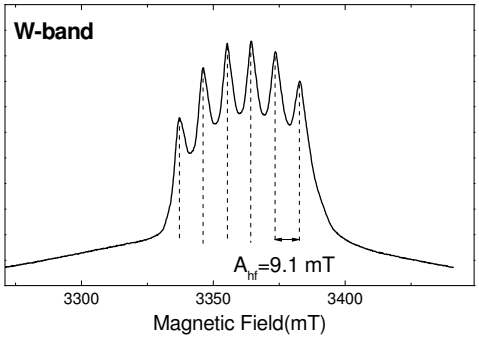

Fig. 1. W-band ESE EPR spectrum of Mn-HAp detected at room temperature. The components of electron-nuclear hyperfine splitting are marked. The position of the spectrum (g-factor) and the value of hyperfine constant A_{hf} are typical for Mn^{2+} ions.

A location (position) of the introduced manganese even in the bulk samples is still debated [51]. As for the natural apatites, two nonequivalent calcium positions Ca(1) and Ca(2) distinguishable in the HAp structure are proposed for the Mn^{2+} substitutions (see Section DFT calculation for details). Experimentally, we washed the prepared samples in KOH and HCl solutions with various pH values, annealed the samples at different conditions and temperatures up to 850 ^{o}C and did not observe any changes of the Mn^{2+} EPR spectrum. This can serve as additional evidence that Mn^{2+} ions we observe are embedded into the HAp lattice.

Our electron-nuclear double resonance (ENDOR) measurements in the W-band reveal the splittings due to the interaction with the neighboring ^{1}H and ^{31}P nuclei with I = ½. The detailed analysis of the similar ENDOR spectra for the Pb^{3+} [27] and NO_3^{2-} [30] paramagnetic impurities in HAp samples allowed us to define their location in the HAp cell precisely. The simple simulations of the experimental ENDOR spectra in the case of Mn^{2+} in HAp nanoparticles match to both calcium positions, and, therefore, the ENDOR spectra (shown as Fig. S1 in ESI) are not discussed in this paper. For the DFT calculations,

we consider models in which the Mn^{2+} ions occupy either Ca(1) or Ca(2) sites.

3.2. EPR and relaxation time measurements in the irradiated samples

In the EPR spectra of the irradiated samples the spectrum of NO_3^{2-} paramagnetic centers is the dominant one. Fig. 2A and 2B present the spectra of NO_3^{2-} obtained in the HAp and Mn-HAp after X-ray irradiation. The observed three line pattern is a typical powder spectrum due to the hyperfine interaction (described by the hyperfine constant of axial symmetry *A*) between the electronic spin with S = ½ and one nuclear spin with I = 1 as a case for ^{14}N. Detailed interpretation of the NO_3^{2-} spectrum in (nano)-HAp samples is given in [29, 30 33]. The signal of Mn^{2+} ions in the EPR spectrum of the irradiated Mn-HAp is manifested as a broad Gaussian line due to unresolved fine structure. No changes in EPR spectra with temperature within the investigated temperature range were noticed.

No significant difference in EPR spectrum of NO_3^{2-} is observed with Mn-codoping. However, the relaxation characteristics (spin-lattice / longitudinal relaxation time T_{1e} and phase-memory / spin-spin / transverse relaxation time T_2^*) of the NO_3^{2-} paramagnetic center change drastically. This is illustrated on Fig. 2C for T_2^* relaxation time (T_2^* decay and T_{1e} recovery curves could be described by the mono-exponential functions) obtained in the magnetic field corresponding to the maximal ESE signal (marked as B_2 on Fig. 2B). It can be seen that the phase memory time of NO_3^{2-} in Mn-HAp dramatically shortens (up to 30 times) tending to the value of T_2^* of Mn^{2+} below 80 K. The modulation of the electron spin echo due to electron-nuclear couplings (ESEEM) reveals only at T < 15 K, its depth is estimated to be less than 10 % of the ESE amplitude and, therefore, ESSEM does not influence the presented results much.

The measured temperature dependencies of the spin-lattice relaxation rates T_1 are quite complicated due to the contributions of different mechanisms and their detailed analysis is beyond the scope of this work. The effect of the Mn-codoping can be illustrated by the data for T = 50 K in X-band: T_{1e}(HAp, 343.5 mT) = 2500(30) μs; T_{1e}(Mn-HAp, 343.5 mT) = 280(5) μs; and T_{1e}(Mn-HAp, 326 mT) = 10(1) μs. Within the studied temperature range $T_1 > 8T_2^*$ and one can exclude the influence of T_1 relaxation mechanisms on T_2^* for the data analysis.

The values of the spin-spin and spin-lattice relaxation times especially at low temperatures (at room temperatures they can be too short to measure them and to track the influence of the neighboring spins) can be sensitive indicators of spin-spin interactions in distance regimes where the lineshape changes of the conventional EPR are too small to detect [52]. The stronger the dipolar interaction the more effectively the relaxation of the fast relaxing spin is communicated to the more slowly-relaxing spin. In the limit of strong interaction the relaxation time for the slowly-relaxing spin becomes equal to that for the rapidly-relaxing spin. Strong influence of Mn^{2+} on the relaxation of NO_3^{2-} indicates that the distances between them are less than (1-2) nm [52] if we account only single inter-ionic interaction.

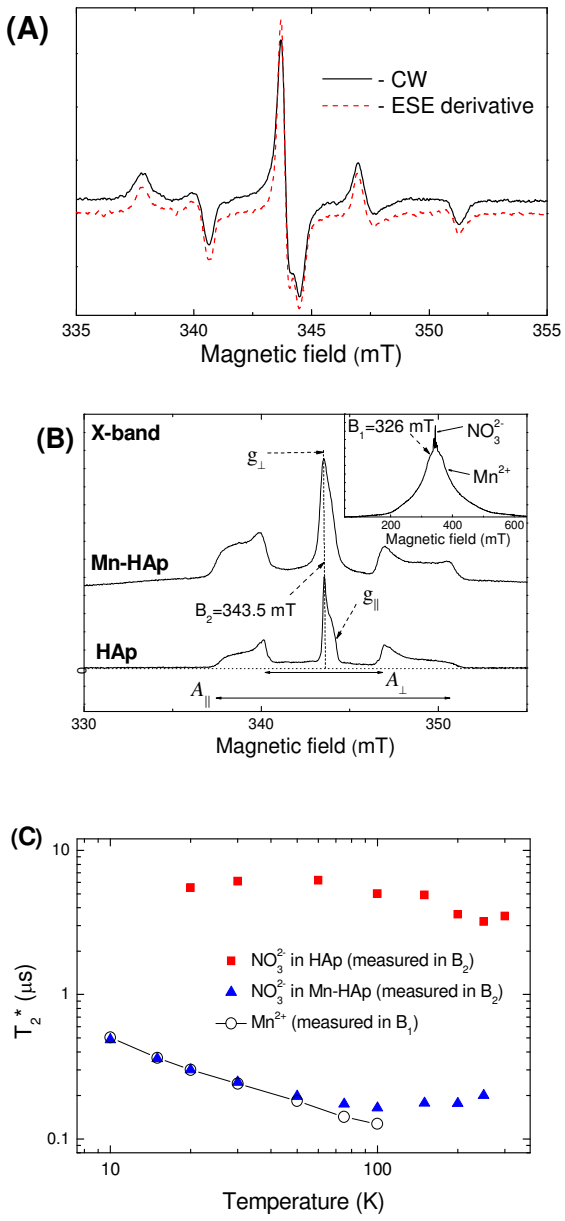

Fig. 2. (A) Comparison of X-band cw (black solid line) and first derivative of ESE EPR (dashed red line) spectra of pure HAp at T = 300 K K after X-ray irradiation. (B) ESE EPR spectra of Mn-HAp (top) and pure HAp (bottom) nanoparticles detected in X-band at T = 50 K after X-ray irradiation in the vicinity of g ≈ 2. The components of the electronic g-factors and electron-nuclear hyperfine constant *A* for NO_3^{2-} are marked. The values of magnetic fields at which the relaxation characteristics of Mn^{2+} and NO_3^{2-} paramagnetic centers were measured are denoted as B_1 and B_2, respectively. Insert shows the ESE EPR spectrum of Mn-HAp in the magnetic field range of (10-600) mT. (C) Temperature dependencies of the phase-memory times T_2^* of NO_3^{2-} paramagnetic center in HAp (triangles), NO_3^{2-} in Mn-HAp (squares) and Mn^{2+} in Mn-HAp (circles).

From the comparison of the integrated intensities of cw and ESE detected EPR spectra of Mn^{2+} and NO_3^{2-} between each other and with the external reference (aqueous solution of CuHis complex) we have estimated the relative number of the ions studied (cf. with the insert in Fig. 2B). From those it follows that $N(Mn^{2+})/ N(NO_3^{2-}) \approx 25(5)$. It implies (assuming the homogeneous distribution of NO_3^{2-}) that not more than one NO_3^{2-} radical can be found in one nano-particle in the investigated species while the number of Mn^{2+} ions can reach the value of about 20 (see section 2.1). Along with the fact that all the observed T_2^* decay and T_{1e} recovery curves are the mono-exponential functions, It leads to the assumption that the Mn^{2+} ions are not randomly distributed in the vicinity of NO_3^- / NO_3^{2-} within nanocrystal. To address this issue, we have performed first-principles calculations presented in the next section.

Probably due to the fast relaxation mechanisms and sufficiently large number of Mn^{2+} ions around the nitrate radical, we could not observe the influence of Mn^{2+} ions on NO_3^{2-} in the attempted ESEEM, ENDOR or electron-electron double resonance (ELDOR, DEER) measurements by using our EPR technique and by applying the standard pulse schemes. It makes it tricky to estimate the interatomic distances and ion distribution directly from the experiment.

3.3. DFT Calculations

Firstly, we have analyzed the thermodynamic stability and the crystallographic surrounding of Mn^{2+} in pure HAp (without addition of nitrate impurity). Basically, we calculate total energy of the 88-atom HAp supercell with a single Mn^{2+} ion incorporated at the various Ca atomic sites. Though the real concentration of Mn^{2+} ions in the investigated species is much lower we believe that this model describes an isolated substitution properly. From a symmetry standpoint, there are two nonequivalent types of Ca(1) site and three types of Ca(2) site in the crystal structure of HAp [3, 9, 15, 46]. We have tested all of these atomic positions. In each case the incorporation of Mn^{2+} leads to appreciable structural deformations associated with the shortening of Mn-O distances compared to Ca-O bonds. The analysis of the calculated energies suggests that Ca(2) sites are energetically more favorable for Mn^{2+} substitution compared to Ca(1) positions. The energy between the Ca(1) substitutional sites and the most stable Ca(2) position is found to be about 0.13 eV, while for the less stable Ca(2) this value is 0.06 eV. The similar results were reported in [14] for Mg^{2+} substitution. The last one has an ionic radius close to that of Mn^{2+}.

For the nitrate-containing HAp we used a model of nitrate defect described in details in [29, 30]. We assume that the impurity substitutes PO_4^{3-} group with charge balancing maintained via removal of the adjacent Ca ion (Fig.3). The position of Ca vacancy is chosen to obtain the lowest ground-state energy of the HAp supercell in the presence of NO_3^- (without Mn^{2+}) only and is fixed throughout the simulations.

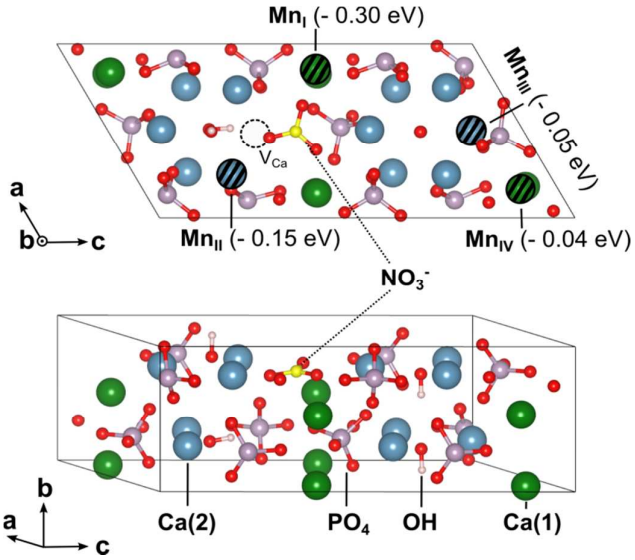

Fig. 3. Optimized geometry of HAp containing NO_3^- defect with schematic illustration of the selected positions of Mn^{2+} considered in the work. The values of binding energy calculated for the displayed Mn^{2+} sites are shown in parentheses (Mn_I and Mn_{II} represent the most stable configurations among Ca(1) and Ca(2) positions, correspondingly). Location of Ca^{2+} vacancy (V_{Ca}) is marked by a dashed circle. Ca(1), Ca(2), P, O, H and N atoms are shown as green, blue, purple, red, white and green spheres, respectively.

To investigate the propensity of NO_3^- and Mn^{2+} substitutions to associate within a supercell, we calculate the binding energy of the pair:

$E_b = E_{tot}(NO_3/Mn) + E_{tot}(HAp) – E_{tot}(NO_3) – E_{tot}(Mn)$,

where $E_{tot}(NO_3)$, $E_{tot}(Mn)$ and $E_{tot}(NO_3/Mn)$ are the total energies of the HAp supercells containing NO_3^- ion, Mn^{2+} ion and both NO_3^- and Mn^{2+}, respectively; $E_{tot}(HAp)$ is the total energy of the same supercell without impurities.

We have compared the values of E_b for different arrangements of NO_3^-/Mn^{2+} pair. The selected configurations are shown on Fig.3. Negative sign of E_b suggests the high probability of substitutions to occupy the corresponding adjacent positions in HAp lattice [52]. The largest values of about –0.3 eV were obtained for Mn^{2+} occupying the Ca(1) sites closest to the nitrate (see Fig.3; Mn_I site; the distance between the manganese and nitrogen centers is $r_{N\text{-}Mn}$ = 0.34 nm). Regarding the case of Mn^{2+} at Ca(2) positions neighboring NO_3^- ion, this also gives the negative values of E_b (around –0.15 eV; Mn_{II} site in Fig.3, $r_{N\text{-}Mn}$ = 0.63 nm). At the same time, the binding energy of about –0.05 eV obtained for the structures with Mn^{2+} located relatively far from NO_3^- within the same supercell indicates somewhat lower energetic gain of the association (Mn_{III} and Mn_{IV} sites in Fig.3, $r_{N\text{-}Mn} \approx 0.85$ nm).

The results indicate thermodynamic preference for simultaneous substitution of oppositely charged Mn^{2+} and NO_3^- ions into HAp lattice, i.e. the impurities are more stable in case of simultaneous incorporation. Since the isolated Mn^{2+} and NO_3^- defects are both charge neutral and the spin density of Mn^{2+} is strongly localized, no contribution of coulombic or magnetic interaction is expected to be involved in the observed effect. Therefore, we suppose that the underlying

mechanism is related only to structural differences, as it was previously suggested in [13] for substitutional Zn^{2+} and Ca-vacancy complex in HAp. In other words, incorporation of the pair compensates the local lattice distortions induced separately by both substitutions, and thereby lowers the total energy of the nanocrystal.

In addition, the revealed presence of energetically preferable manganese sites in the vicinity of the anionic impurity suggests that certain content of nitrate in HAp can lead to non-uniform distribution of Mn^{2+} ions within nanocrystal. In turn, this can alternate the pathways of Mn^{2+} ions release into host media and the mechanisms of surface resorption, thereby influencing osteoconductivity of the material. On the other hand, due to the energetic preference of co-substitution the lattice of manganese doped HAp can become more labile for incorporation of undesired impurities (which in turn can have a cytotoxic effect) as compared to that of pure crystal.

In principle, one can also expect a similar effect to take place in case of other pair of substitutions (e.g. carbonate with some transition metal) instead of the nitrate and manganese. To support this idea further experimental and computational analysis should be carried out.

Conclusions

Quite a simple approach based on pulsed EPR is shown to investigate simultaneous doping of HAp nanoparticles by manganese and nitrate. To our knowledge, the work provides the first direct experimental evidence of interplay between oppositely charged ionic additives in nanosized HAp supported by first-principles calculations.

The main outcome of the work can be summarized as follows:

1. Measurements of electron spin relaxation times allowed observing simultaneous incorporation of manganese and nitrate substituions into the HAp nanoparticle. Due to the high sensitivity, the EPR spectroscopy could be applicable for further research with the lower levels of impurities and smaller sizes of nanocrystals.
2. Performed *ab initio* analysis clearly indicates that it needs less energy to incorporate both manganese and nitrate into the HAp lattice simultaneously than to insert the separate impurities. Thereby it supports the feasibility of HAp co-doping.
3. The results of the EPR measurements and calculations suggest preferably non-uniform arrangement of Mn^{2+} ions within HAp nanocrystal in presence of nitrate impurity. In turn, this effect can have a direct impact on the functional properties of the material (such as ion exchange with environment, surface resorption, etc).

Acknowledgements

This work was funded by the subsidy allocated to Kazan Federal University for the state assignment in the sphere of scientific activities. M.G. acknowledges the subsidy of the Russian Government to support the Program of competitive Growth of Kazan Federal University among World's Leading Academic Centers. E.K and V.P. acknowledge partial support from Lomonosov Moscow State University Program of Development and Russian Foundation for Basic Research.

Notes and References

1 S. Dorozhkin and M. Epple, *Angew Chem Int Ed*, 2002, **41**, 3130.
2 E. Landi, G. Celotti, G. Logroscino and A. Tampieri, *J Eur Cer Soc,* 2003, **23**, 2931.
3 H. Zhou and J.Lee, *Acta Biomaterialia*, 2011, **7**, 2769.
4 A. Tabaković, M.Kester and J. Adair, *Wiley Interdisciplinary Reviews: Nanomedicine and Nanobiotechnology*, 2012, **4**, 96.
5 F. Chen, P. Huang, Y.Zhu, J. Wu, C.Zhang and D. Cui, *Biomaterials,* 2011, **32**, 9031.
6 K. Ramesh, E. Ling, C. Gwie, T. White and A. Borgna, *J Phys Chem C*, 2012, **116**, 18736.
7 H.Sun, F.Su, J. Ni, Y.Cao, H.He and K. Fan, *Angew Chem Int Ed*, 2009, **48**, 4390.
8 Q.Y. Ma, S. Traina, T.J. Logan and J. Ryan, *Envir Sci Tech,* 1993, **27**, 1803.
9 S. Kehoe, *Optimisation of hydroxyapatite (HAp) for orthopaedic application via the chemical precipitation technique.* Ph.D. Thesis, Dublin: City University, 2008, 393 p.
10 K. Matsunaga, H. Inamori and H. Murata, *Phys Rev B,* 2008, **78**, 094101.
11 T. Suzuki, T. Hatsushika and M. Miyake, *J Chem Soc, Faraday Trans*, 1982, **78**, 3605.
12 I.R. de Lima, G.G. Alves, C.A. Soriano, A.P. Campaneli, T.H.Gasparoto, E.S.Ramos, L.A. de Sena, A.M. Rossi and J.M. Granjeiro, *J Biomed Mat Res Part A*, 2011, **98**, 351.
13 K. Matsunaga, H. Murata, T. Mizoguchi and A. Nakahira, *Acta Biomaterialia*, 2010, **6**, 2289.
14 D. Laurencin, N. Almora-Barrios, N.H. De Leeuw, C. Gervais, C. Bonhomme, F. Mauri, W.Chrzanowski, J.C. Knowles, R.J. Newport, A. Wong, Z. Gan and M.E. Smith, *Biomaterials*, 2011, **32**, 1826.
15 I.R. Gibson and W. Bonfield, *J Mater Sci Mater Med*, 2002, **13**, 685.
16 G.S. Kumar, E.K. Girija, A. Thamizhavel, Y. Yokogawa and S.N. Kalkura, *Mater Chem Phys,* 2012, **134**, 1127.
17 E. Landi, S. Sprio, M. Sandri, G. Celotti and A. Tampieri, *Acta Biomaterialia*, 2008, **4**, 656.
18 M. Moreira, V. Da Silva Aragao, G. De Almeida Soares and E. Dos Santos, *Key Eng Mat,* 2012, **493-494**, 20,
19 J. R. Chelikowsky, M. Alemany, T.L. Chan and G. M. Dalpian, *Rep. Prog. Phys.*, 2011, **74**, 046501.
20 D.J. Norris, A.L. Efros and S.C. Erwin, *Science*, 2008, **319**, 1776.
21 B. Sutter, T. Wasowicz, T. Howard, L.R. Hossner and D.W. Minge, *Soil Sci Soc Amer Journ*, 2002, **66**, 1359.
22 M. Mengeot, R.H. Bartram and O.R. Gilliam, *Phys Rev B*, 1975, **11**, 4110.
23 F. Callens, G. Vanhaelewyn, P. Matthys and E. Boesman, *Appl Magn Reson*, 1998, **14**, 235.
24 P. Moens, F. Callens, S. Van Doorslaer and P. Matthys, *Phys Rev B*, 1996, **53**, 5190.
25 D.U. Schramm, J. Terra, A.M. Rossi and D.E. Ellis, *Phys Rev B*, 2000, **63**, 024107.
26 M.R. Gafurov, B.V. Yavkin, T.B. Biktagirov, G.V. Mamin, S.B. Orlinskii, V.V. Izotov, M.Kh. Salakhov, E.S.

Klimashina, V.I. Putlayev, V.A. Abdulyanov, I.M. Ignatjev, R.N. Khairullin, A.V. Zanmochkin and Yu. A. Chelyshev, *Magn.Reson. Solids*, 2013, **15**, 13102.
27 B.V. Yavkin, G.V. Mamin, S.B. Orlinskii, M.R. Gafurov, M.Kh. Salakhov, T.B. Biktagirov, E.S. Klimashina, V.I. Putlayev, Y.D. Tretyakov and N.I. Silkin, *Phys Chem Chem Phys*, 2012, **14**, 2246.
28 T.B. Biktagirov, M.R. Gafurov, G.V. Mamin, S.B. Orlinskii, B.V. Yavkin, A.A. Rodionov, E.S. Klimashina, V.I. Putlyaev and Y.Y. Fillipov, *Optics and Spectroscopy*, 2014, **116**, 715-720
29 T. Biktagirov, M. Gafurov, G. Mamin, E. Klimashina, V. Putlayev and S. Orlinskii, *J Phys Chem A*, 2014, **118**, 1519.
30 M.R. Gafurov, T.B. Biktagirov, B.V. Yavkin, G.V. Mamin, Y.Y. Filippov, E.S. Klimashina, V.I. Putlayev and S.B. Orlinskii, *JETP Lett*, 2014, **99**, 196.
31 S. Bose, G. Fielding, S. Tarafder and A. Bandyopadhyay, *Trends Biotechnol*, 2013, 31, 594.
32 I.P. Vorona, S.S. Ishchenko, N.P. Baran, V.V. Rudko, I.V. Zatovskii, N.A. Gorodilova and V.Y.Povarchuk, *Phys Solid State*, 2010, **52**, 2364.
33 M. Gafurov, T. Biktagirov, G. Mamin and S. Orlinskii, *Appl Magn Reson*, 2014, **45**, 1189.
34 E.S.Kovaleva, M.P. Shabanov, V.I. Putlayev, Ya.Ya. Filippov, Y.D. Tretyakov and V.K. Ivanov, *Mat wiss u Werkstofftech*, 2008, **39**, 822.
35 T. De Keijser, J.I. Langford, E.J. Mittemeijer and A.B.P. Vogels, *J Appl Cryst*, 1982, **15**, 3087.
36 J.P. Perdew, K. Burke and M. Ernzerhof, *Phys Rev Lett*, 1996, **77**, 3865.
37 D. Vanderbilt, *Phys Rev B*, 1990, **41**, 7892.
38 P. Giannozzi at eal., *J Phys Condens Matter*, 2009, **21**, 395502.
39 H.J. Monkhorst and J.D.Pack, *Phys Rev B*, 1976, **13**, 5188.
40 M. Yashima, Y. Yonehara and H. Fujimori, *J Phys Chem C*, 2011, **115**, 25077.
41 V.I. Anisimov, J. Zaanen and O.K. Andersen, *Phys Rev B,* 1991, **44**, 943.
42 M. Cococcioni and S. De Gironcoli, *Phys Rev B*, 2005, **71**, 035105.
43 H.J. Kulik, M. Cococcioni, D.A.Scherlis and N. Marzari, *Phys Rev Lett*, 2006, **97**, 103001.
44 T.O. Strandberg, C.M. Canali and A.H. MacDonald, *Phys Rev B,* 2009, **80**, 024425.
45 J. Low, *Phys Rev*, 1957, **105**, 793.
46 L.G. Gilinskaya and M.J. Sherbakova, *Isomorphous substitution and structural defects in apatites as found by EPR investigation.* In: V.S. Sobolev, editor. *Physics of apatite. (Spectroscopic investigation of apatite).* Novosibirsk: Publishing House "Nauka", Siberian Branch. 1975, pp. 7-62 (in Russian)
47 I. Mayer, H. Diab, D. Reinen and C. Albrecht, *J Mater Sci,* 1993, **28**, 2428.
48 M.L. Praamsma and P.J. Parsons, *J Anal At Spectrom*, 2014, **29**, 1243.
49 Y. Pan, N. Chen, J.A. Weil and M.J. Nilges, *Amer Miner*, 2002, **87**, 1333.
50 M. Markovic, B.O. Fowler and M.S. Tung, *J Res Natl Inst Stand Technol*, 2004, **109**, 553.
51 W. Pon-On, S. Meejoo and I. Tang, *Mater Res Bull*, 2008, **43**, 2137.
52 S.S. Eaton and G.R. Eaton, *Distance Measurements by CW and Pulsed EPR.* In: L.J. Berliner, S.S. Eaton and G.R. Eaton, editors. *Distance measurements in biological systems by EPR (Biological Magnetic Resonance V. 19).* New-York: Kluwer Academic Publishing, 2002, pp. 1-27
53 C.G. Van de Walle and J. Neugebauer, *J Appl Phys*, 2004, **95**, 3851.